NeuroImage 196 (2019) 337–350

Contents lists available at ScienceDirect

NeuroImage

journal homepage: www.elsevier.com/locate/neuroimage

Dependence of resting-state fMRI fluctuation amplitudes on cerebral cortical orientation relative to the direction of B0 and anatomical axes

Olivia Viessmann [a,*], Klaus Scheffler [b], Marta Bianciardi [a], Lawrence L. Wald [a,c], Jonathan R. Polimeni [a,c]

[a] Athinoula A. Martinos Center for Biomedical Imaging, Department of Radiology, Harvard Medical School, Massachusetts General Hospital, 149 13th St., Charlestown, Boston, MA 02129, USA
[b] Max Planck Institute for Biological Cybernetics, Max-Planck-Ring 11, 72076 Tübingen, Germany
[c] Harvard-Massachusetts Institute of Technology, Division of Health Sciences and Technology, Cambridge, MA, USA

ARTICLE INFO

Keywords:
Resting-state fMRI
BOLD
Orientation effects
High resolution
Laminar fMRI

ABSTRACT

Functional magnetic resonance imaging (fMRI) is now capable of sub-millimetre scale measurements over the entire human brain, however with such high resolutions each voxel is influenced by the local fine-scale details of the cerebral cortical vascular anatomy. The cortical vasculature is structured with the pial vessels lying tangentially along the grey matter surface, intracortical diving arterioles and ascending venules running perpendicularly to the surface, and a randomly oriented capillary network within the parenchyma. It is well-known that the amplitude of the blood-oxygenation level dependent (BOLD) signal emanating from a vessel depends on its orientation relative to the B_0-field. Thus the vascular geometric hierarchy will impart an orientation dependence to the BOLD signal amplitudes and amplitude differences due to orientation differences constitute a bias for interpreting neuronal activity. Here, we demonstrate a clear effect of cortical orientation to B_0 in the resting-state BOLD-fMRI amplitude (quantified as the coefficient of temporal signal variation) for 1.1 mm isotropic data at 7T and 2 mm isotropic at 3T. The maximum bias, i.e. the fluctuation amplitude difference between regions where cortex is perpendicular to vs. parallel to B_0, is about +70% at the pial surface at 7T and +11% at 3T. The B_0 orientation bias declines with cortical depth, becomes progressively smaller closer to the white matter surface, but then increases again to a local maximum within the white matter just beneath the cortical grey matter, suggesting a distinct tangential network of white matter vessels that also generate a BOLD orientation effect. We further found significant (negative) biases with the cortex orientation to the anterior-posterior anatomical axis of the head: a maximum negative bias of about −30% at the pial surface at 7T and about −13% at 3T. The amount of signal variance explained by the low frequency drift, motion and the respiratory cycle also showed a cortical orientation dependence; only the cardiac cycle induced signal variance was independent of cortical orientation, suggesting that the cardiac induced component of the image time-series fluctuations is not related to a significant change in susceptibility. Although these orientation effects represent a signal bias, and are likely to be a nuisance in high-resolution analyses, they may help characterize the vascular influences on candidate fMRI acquisitions and, thereby, may be exploited to improve the neuronal specificity of fMRI.

1. Introduction

Since the initial demonstration of the blood-oxygenation-level-dependent (BOLD) signal (Ogawa et al., 1990) and its application to measuring brain activity with MRI (Kwong et al., 1992; Bandettini et al., 1992; Ogawa et al., 1993), BOLD-based functional magnetic resonance imaging (fMRI) has become the most widely used tool to measure activity throughout the entire human brain non-invasively. Because the fMRI signals all provide indirect measures of neuronal activity through tracking haemodynamic responses (such as changes in blood oxygenation, flow, or volume), substantial effort has been directed towards improving the neuronal specificity of fMRI so that it more faithfully reflects neuronal activity. Improved spatial and temporal specificity of fMRI has been achieved through advances in instrumentation, pulse

* Corresponding author.
E-mail addresses: oviessmann@mgh.harvard.edu (O. Viessmann), Klaus.Scheffler@tuebingen.mpg.de (K. Scheffler), martab@mgh.harvard.edu (M. Bianciardi), wald@nmr.mgh.harvard.edu (L.L. Wald), jonp@nmr.mgh.harvard.edu (J.R. Polimeni).

https://doi.org/10.1016/j.neuroimage.2019.04.036
Received 11 December 2018; Received in revised form 30 March 2019; Accepted 11 April 2019
Available online 17 April 2019

sequence, and image reconstruction (Polimeni and Wald, 2018). A better understanding of the relationship between the fMRI signals and the underlying microvasculature and neuronal activity has been achieved through a combination of biophysical modelling (Boxerman et al., 1995; Bandettini and Wong, 1995; Boas et al., 2008; Uludag et al., 2009) and invasive microscopy of microvascular dynamics (Kleinfeld et al., 1998; Hillman et al., 2007; Tian et al., 2010).

Recently, these *in vivo* measurements of microvascular anatomy and dynamics have been combined with the biophysical modelling of the fMRI signals to provide a more accurate picture of how the BOLD signal arises from the haemodynamic responses to neuronal activity (Gagnon et al., 2015, 2016; Báez-Yánez et al., 2017). While the results from these studies using anatomically accurate reconstructions of cortical microvascular geometry and topology generally agree with results from previous studies using simplified approximations of vessels as random cylinders (Boxerman et al., 1995; Uludag et al., 2009), several new insights were gained using these realistic vascular models. The BOLD signal arises from deoxyhaemoglobin in the blood that induces susceptibility offsets around and inside the vessels that scale with vessel orientation. The former extravascular component is maximised when the vessel is perpendicular to the main magnetic field, B_0, but vanishes when the vessel is exactly parallel to B_0; whereas the latter intravascular component is maximised for a vessel with parallel alignment to B_0 and disappears in perpendicular alignment to B_0 (Buxton, 2009). Gagnon et al. (2015) demonstrated—both through simulations based on reconstructions of mouse cortical microvasculature and through experimental data acquired in humans at 3Tesla (3T) with a hypercapnia challenge (via CO_2 gas inspiration)—that the BOLD signal change amplitude was 40% larger in voxels sampling locations where the cortical surface normal was parallel to the direction of B_0 (i.e. with pial vessels perpendicular to B_0) compared to voxels that were sampling location where the cortical surface normal was perpendicular to B_0 (i.e. with pial vessels randomly oriented to B_0). This phenomenon therefore induces a substantial bias in the BOLD fMRI signal that, for a given neuronal activity amplitude, varies systematically with cortical geometry. This orientation effect of the BOLD signal has been investigated in subsequent studies (Báez-Yánez et al., 2017; Kennel et al., 2017; Fracasso et al., 2018).

Sampling with higher spatial resolution increases the vascular heterogeneity across voxels and thereby enhances these orientation biases. As fMRI technologies continue to improve, and voxel sizes decrease to scales far smaller than the thickness of the cortical ribbon, each individual voxel will increasingly sample from one level of the vascular hierarchy—i.e. voxels will sample from the large-sized pial veins tangential to the cortex, the mid-sized intracortical ascending venules, or the small-sized parenchymal capillaries. Furthermore, it is well-known that at higher magnetic field strengths, the intravascular contributions of the BOLD signal diminish while the extravascular contributions amplify (Boxerman et al., 1995; Bandettini and Wong, 1995). The extravascular BOLD contributions are spatially spread out in contrast to the localised intravascular components. At field strength of 7Tesla (7T) and above, the extravascular BOLD contributions dominate (Ugurbil et al., 1999), and therefore it is expected that the orientation effect will be far more pronounced.

Here we investigate the sensitivity bias in resting-state fMRI (rs-fMRI) based on gradient-echo BOLD imposed by the relative orientation of the cortical surface normal vector and B_0, as well as the anatomical axes of the brain. We analyse the effect with echo-planar-imaging (EPI) data at high resolution (1.1 mm isotropic) at 7T and moderate resolution (2 mm isotropic) at 3T. We confirm that cortical orientation biases can be seen in the amplitudes of rs-fMRI fluctuations across the entire cerebrum, and that—because the effect appears to be predominantly driven by pial vasculature—these effects vary systematically with cortical depth (Viessmann et al., 2018).

The source of the cortical orientation dependence of the BOLD fMRI signal originates in the susceptibility effect. However, not all signal contributions to the gradient-echo time-series data, in particular physiological signals, are driven by susceptibility changes due to the BOLD response (Krüger and Glover, 2001; Kundu et al., 2014). Therefore we expect that different contributors to the rs-fMRI fluctuations vary in their level of relative contributions to this orientation effect. To test this, we also quantified the percentage of the signal variance explained by low frequency drift, motion parameters, respiratory and cardiac signals from physiological recordings as a function of cortical orientation and cortical depth.

2. Theory

2.1. Effects of vessel orientation relative to the main magnetic field B_0

The offsets in local magnetic fields induced by spatially-varying magnetic susceptibility are well-known to depend on the orientation of the structures that induce the variation in susceptibility. This "tensorial" nature of the relation between susceptibility and the resulting offset in magnetic field has been shown to introduce a dependence of T_2^* values on the orientation of white matter fibre bundles (Bender and Klose, 2010; Lee et al., 2011; Oh et al., 2013) and is also seen in cartilage (Hänninen et al., 2017). Further, the cortical microarchitecture has been shown to exhibit aT_2^* orientation dependence to the B_0 axis (Cohen-Adad et al., 2012).

The cerebral cortical vasculature follows a strict geometry relative to the cortex, which is well-known from classic anatomy studies by Pfeifer (1928) and detailed in the microscopy work of Duvernoy et al. (1981). The largest-sized vessels (the pial arteries and veins) lie tangentially along the surface, medium-sized intracortical vessels (diving arterioles and ascending venules) run perpendicularly to the surface, and the smallest-sized vessels (the capillaries) are randomly oriented within the parenchyma (see Fig. 1).

Biophysical models for the resonance frequency shifts induced by a change in magnetic susceptibility ($\Delta\chi$) typically approximate a single blood vessel with an infinitely-long cylinder, with extra- and intravascular offsets represented by ω_{extra} and ω_{intra}, and are defined as

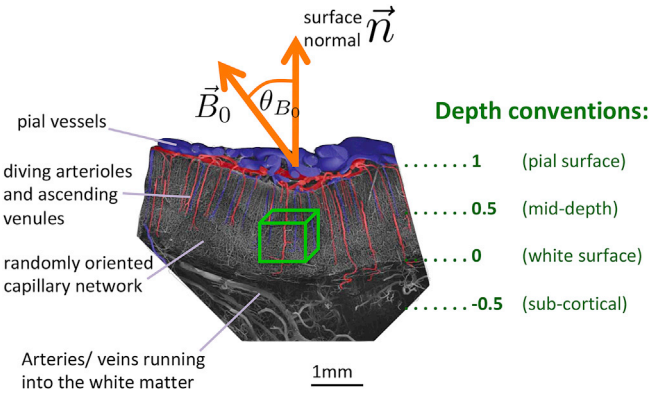

Fig. 1. Schematic overview of the geometry of cortical blood vessels, and the cortical depth convention used in this work. At a given cortical location, pial vessels are found running tangentially along the surface, and diving arterioles and ascending venules run perpendicular to the surface. Of these perpendicular vessels the *principal vessels* pass through the cortical grey matter, enter into the white matter, and typically bend near the grey-white interface as they traverse into the distal white matter (electron micrograph from macaque monkey cortex, reproduced from Hirsch et al. (2012) with permission, and annotated with descriptions). A millimetre-size voxel (depicted as a green box) is likely to contain only a subset of the vasculature. The pial surface is denoted as depth = 1, the mid-grey at half cortical thickness is denoted as depth = 0.5, and the grey/white matter interface (white surface) as depth = 0. Sub-cortical depths are denoted by negative depth values. Cortical orientation θ_{B_0} is defined as the angle between the surface normal vector $\vec{n}$ and the B_0 axis $\overrightarrow{B_0}$.

$$\omega_{\text{extra}} \propto \Delta\chi\omega_0 \left(\frac{a}{r}\right)^2 \cos(2\phi)\sin^2(\vartheta_{B_0,\text{vessel}}) \text{ and} \quad (1)$$

$$\omega_{\text{intra}} \propto \Delta\chi\omega_0 \left(3\cos^2(\vartheta_{B_0,\text{vessel}}) - 1\right) \quad (2)$$

where $\vartheta_{B_0,\text{vessel}}$ is the angle between the cylinder's main axis and the direction of the B_0 axis, a is the vessel diameter, $\vec{r}$ is the position vector, with $r = ||\vec{r}||$ the distance to the centre of the cylinder, and ϕ is the angle between the position vector $\vec{r}$ and the in-plane component of B_0 (Ogawa et al., 1993; Yablonskiy and Haacke, 1994; Haacke et al., 2009). Both the extra- and intravascular components of the BOLD signal exhibit a dependence on $\vartheta_{B_0,\text{vessel}}$ and thus have an orientation dependence (Bandettini and Wong, 1995). While the dependence on $\vartheta_{B_0,\text{vessel}}$ is well-known, it is typically neglected in fMRI data analysis (Menon, 2002). The justification for ignoring this effect has been the assumption that the vessel network is random with uniform angular distribution or that orientation effects average out with conventional voxel sizes of a few millimetres (Ogawa et al., 1993; Uludag et al., 2009).

Note that the angle $\vartheta_{B_0,\text{vessel}}$ here represents the orientation of the *vessel* relative to the B_0 axis, whereas to simplify our treatment of orientation effects we use the angle θ_{B_0} to represents the orientation of the *cortical surface normal* relative to the B_0 axis as shown in Fig. 2. The gradient-echo BOLD signal is known to be dominated by large veins and so changes in this BOLD signal will primarily be driven by pial vessels that lie tangentially on the surface, i.e. the pial vessel axis is perpendicular to the cortical surface normal and so for these vessels $\vartheta_{B_0,\text{vessel}} = \pi/2 - \theta_{B_0}$ by definition, and it follows that for pial vessels $\sin(\vartheta_{B_0,\text{vessel}}) = \sin(\pi/2 - \theta_{B_0}) = \cos(\theta_{B_0})$. Thus for the gradient-echo BOLD signal variation as a function of cortical surface normal orientation θ_{B_0} —including the extra- and intravascular BOLD changes $\Delta\text{BOLD}_{\text{extra}}$ and $\Delta\text{BOLD}_{\text{intra}}$—we expect that

$$\Delta\text{BOLD}_{\text{extra}} \propto \cos^2(\theta_{B_0}) \text{ and} \quad (3)$$

$$\Delta\text{BOLD}_{\text{intra}} \propto \sin^2(\theta_{B_0}) \quad (4)$$

due to the pial vessel dominance of the gradient-echo BOLD signal. At field strengths above about 4T the BOLD signal is dominated by the extravascular component (Ugurbil et al., 1999; Uludag et al., 2009), i.e. the signal changes are predominantly driven by changes in the susceptibility-induced field offsets surrounding the vessels, because intravascular T_2 values are smaller than tissue T_2 values and therefore the intravascular signal becomes negligible for echo times (TE) that optimize functional CNR (Duong et al., 2003). Hence, vessel orientation-dependent signal dependency at ultra-high fields ($\geq$ 7T) should follow the $\cos^2(\theta_{B_0})$ term in Eq. (3) closely. When a given cortical location, as depicted in Fig. 2, is oriented parallel to B_0 (θ_{B_0}=0°), i.e. when the cortical surface normal is parallel to B_0, all pial vessels will lie in a plane that is perpendicular to the B_0axis and thus their contribution to the extravascular frequency shift is maximised. At this same cortical location, the diving arterioles and ascending venules will be parallel to B_0(because they are parallel to the cortical surface normal) and thus at this cortical location their signal contribution is minimised. In the opposite configuration—locations where the cortical surface normal is oriented perpendicular to B_0 (θ_{B_0}=90°)—the pial vessels, which run in arbitrarily directions tangential to the cortical surface, will in general exhibit a uniform distribution of orientations and will not have a preferred orientation relative to B_0. In this cortical location, the extravascular frequency shift from the pial vessels will be at a minimum (but not zero), while the diving vessels will consistently run perpendicular to the direction of B_0 and therefore their extravascular fields will be maximised. In summary, at ultra-high fields, where the BOLD signal is predominantly extravascular, we expect the BOLD signal from pial vessels to be maximal in regions where cortex normal is oriented parallel to B_0 and minimal where cortex normal is perpendicular to B_0, whereas BOLD signal from ascending venules will be minimal in regions where the cortex normal is parallel to B_0 and maximal where the cortex normal is perpendicular to B_0.

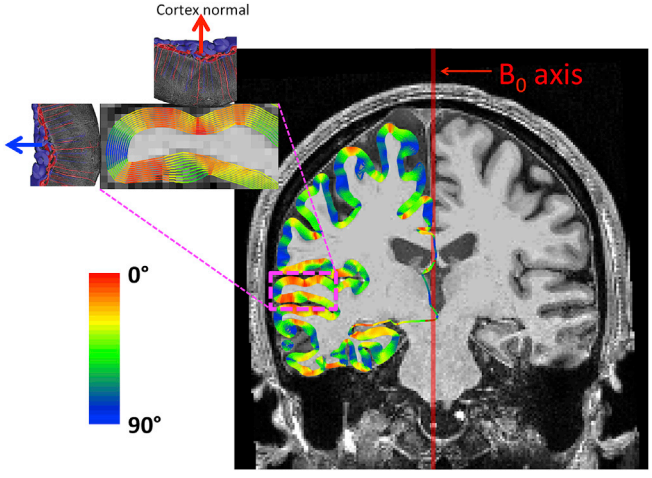

Fig. 2. Schematic overview of cortical orientation relative to B_0 and the configuration of the cortical vasculature. The orientation of the cortical surface normal relative to the direction of the B_0 axis changes smoothly across the brain with cortical folding; this orientation is color-coded as red (0°) to blue (90°), and the axis of the B_0 field is denoted by the red bar. A zoomed-in view of a cortical fold is presented in the left upper corner, depicting the orientation of the vessels for both the cases of the cortical surface normal being parallel and perpendicular relative to the B_0 axis. (The cortical segment is the same electron micrograph from macaque monkey cortex shown in Fig. 1.)

2.2. Orientation effects along other axes

While the cortical surface orientation relative to the B_0 axis is expected to have an effect on the BOLD signal, we also tested for biases along other axes. Our original aim was to further test for potential biases along the phase-encoding (PE) axis of the EPI echo train due to enhanced T_2^*-blurring and geometric distortion along that low-bandwidth direction. At cortical locations where the cortical surface normal is parallel to the PE direction, there may be radial smoothing (i.e. in the direction perpendicular to the cortical surface) and distortion imposed in the EPI data, leading to a reduction in BOLD fluctuations as signals get smoothed across pial, cerebrospinal fluid (CSF) and grey matter compartments. At locations where the cortical surface normal is perpendicular to the PE direction, there may be tangential smoothing, leading to a weaker reduction in BOLD fluctuations as signals are smoothed within tissue compartments. Typical EPI acquisitions are prescribed transverse to the brain in which case the anterior-posterior anatomical axis of the brain coincides with the PE axis of the imaging, the right-left axis coincides with the readout (RO) direction, and the head-foot axis coincides with the slice-select (SS) direction. To determine if a bias is due to the direction of the PE axis we acquired one control data set that had the PE and RO axes exchanged such that the PE axis was aligned to the anatomical right-left axis. We calculated expected voxel blurring and voxel displacement values for the 7T data, see Supplementary Material 1. Similarly there may be blurring along the SS axis due to imperfect slice profiles and spin history effects due to movement along that direction. Therefore to test this we further acquired one control data set that had the RO and SS axes swapped by acquiring the EPI slices in a sagittal orientation. This allowed us to control for potential blurring effects in the SS direction contributing to the observed B_0-related orientation bias, as these axes (SS and B_0) are closely aligned in axial acquisitions with the typical head-first supine positioning of the subject in the MR scanner.

3. Methods

3.1. MR data

3.1.1. 7T

MR data were acquired, after obtaining informed consent, within 13 healthy subjects using a whole-body 7T scanner (Magnetom, Siemens Healthineers, Germany) with a custom-built 32-channel receive coil head array and a single-channel band-pass birdcage volume coil for transmit (Keil et al., 2010). As a primary data set, 5 subjects were scanned with axially-acquired EPI, and, as a control data set, 8 subjects were scanned with sagittally-acquired EPI. Because the axially-acquired data are the primary data, unless otherwise noted, by default all results refer to the axially-acquired data.

Axial EPI: Each session consisted of 6 runs of rs-fMRI with gradient-echo SMS-EPI with an isotropic voxel size of 1.1 mm, matrix = 174 × 174 × 87, number of time points per run = 160, SMS = 3 (FOV/3 CAIPI shift) (Setsompop et al., 2012), GRAPPA = 4 (96 reference lines) with FLEET ACS of 10° (Polimeni et al., 2015), no partial Fourier, TR = 1700 ms, TE = 26 ms, FA = 65°, nominal echo-spacing = 0.79 ms, PE bandwidth (BW) = 29 Hz/pixel, RO BW = 1512 Hz/pixel, PE direction = anterior-to-posterior; RO direction = right-to-left.

Sagittal EPI (control data set): Each session consisted of 3 runs of rs-fMRI with gradient-echo SMS-EPI with an isotropic voxel size of 1.2 mm, matrix = 160 × 160 × 126, number of time points per run = 100, SMS = 2 (FOV/2 CAIPI shift) (Setsompop et al., 2012), GRAPPA = 4 (128 reference lines) with FLEET ACS of 10° (Polimeni et al., 2015), no partial Fourier, TR = 3500 ms, TE = 23 ms, FA = 80°, nominal echo-spacing = 0.76 ms, PE BW = 33 Hz/pixel, RO BW = 1562 Hz/pixel, PE direction = anterior-to-posterior; RO direction = head-to-feet.

T_1-weighted (T_1-w) scan: Each session acquired a multi-echo magnetization-prepared rapid gradient echo (MEMPRAGE) (van der Kouwe et al., 2008) with an isotropic voxel size of 0.75 mm, matrix = 320 × 320 × 224, GRAPPA = 2 (32 reference lines), TI/TR = 1100/2530 ms, TE_1/TE_2 = 1.76/3.7 ms, 13 ms adiabatic FOCI pulse Hurley et al. (2010) with FA = 5°, no partial Fourier, BW = 651 Hz/pixel, echo-spacing = 6.2 ms. These data were used as an anatomical reference as described recently (Zaretskaya et al., 2018).

Physiological recordings were logged only during the axial EPI scans using a piezoelectric sensor placed on the volunteer's finger for the cardiac trace and a respiratory bellow around the volunteer's chest for the respiratory trace.

3.1.2. 3T

MR data were acquired, after obtaining informed consent, within 10 healthy subjects on a whole-body 3T scanner (Prisma, Siemens Healthineers, Germany) using a vendor-supplied 64-channel receive coil head-neck array and a standard single-channel body coil for transmit. All EPI scans were acquired with axial orientation.

Axial EPI: For 7 out of the 10 subjects, each session consisted of 3 runs of rs-fMRI with gradient-echo SMS-EPI with an isotropic voxel size of 2 mm, matrix = 128 × 128 × 60, number of time points per run = 120, SMS = 2 (FOV/2 CAIPI shift) (Setsompop et al., 2012), GRAPPA = 2 (24 reference lines) with FLEET ACS of 10° (Polimeni et al., 2015), no partial Fourier, TR = 2000 ms, TE = 29 ms, FA = 74°, nominal echo-spacing = 0.6 ms, PE BW = 26 Hz/pixel, RO BW = 1954 Hz/pixel, PE direction = anterior-to-posterior.

Axial EPI with PE exchange (control data set): For 3 out of the 10 subjects an additional set of 3 runs was acquired with the PE direction exchanged to run along the right-to-left direction. For these scans the EPI protocol had to be changed slightly with an increased effective echo spacing of 0.65 ms and a BW of 1776 Hz/pixel (all other parameters as above) as it was not possible to achieve the same echo train settings for phase-encoding along right-left due to peripheral nerve stimulation constraints.

A standard B_0fieldmap was acquired to be used for EPI distortion correction.

T_1-w scan: Each session acquired a MEMPRAGE (van der Kouwe et al., 2008) with an isotropic voxel size of 1 mm, matrix = 256 × 256 × 192, GRAPPA = 2 (32 reference lines), TI/TR = 1100/2530 ms, $TE_1/TE_2/TE_3/TE_4$ = 1.69/3.55/5.41/7.27 ms, FA = 7°, no partial Fourier, BW = 650 Hz/pixel, echo-spacing = 9.8 ms.

3.2. Post-processing

3.2.1. Cortical surface reconstruction

The T_1-w images were bias-field corrected using SPM12 (Ashburner et al., 2014) and automatic cortical surface reconstructions were generated using FreeSurfer (Fischl, 2012) with the recon-all pipeline. This generates two surface meshes that define the inner and outer boundaries of the cortical grey matter ribbon—the white surface at the grey/white matter interface and the pial surface at the grey-matter/CSF interface. These surface meshes are isomorphic, i.e. a vertex in the white surface has a bijective correspondence to a vertex in the pial surface. Nine intermediate intra-cortical surfaces and nine surfaces below the white surface were subsequently created with FreeSurfer's mris_expand command (Polimeni et al., 2010, 2018), for a total of 20 surfaces per cortical hemisphere.

3.2.2. Surface normals

The aim was to assign a meaningful surface normal vector to each vertex (Meyer et al., 2003; Cohen-Adad et al., 2012). Because a vertex in a discrete mesh is a 0-dimensional feature, its surface normal is not well-defined. However, an approximation of a normal to the surface at the location of a vertex is given by the area-weighted sum of the normals of the triangular faces incident to the vertex (Meyer et al., 2003) as depicted in Fig. 3.

3.2.3. EPI data preprocessing

The EPI data were slice-time corrected first with sinc interpolation (using FSL's slice timer separately on each SMS slice group) and motion corrected afterwards using AFNI's 3dvolreg which uses polynomial interpolation. Motion parameters were saved for subsequent use as nuisance regressors. The 3T data were distortion corrected using standard B_0 fieldmap-based correction (Jezzard and Balaban, 1995) as implemented by the FSL routines prelude and fugue (Jenkinson, 2004). The 7T data were temporally smoothed by a moving average over 5 TRs

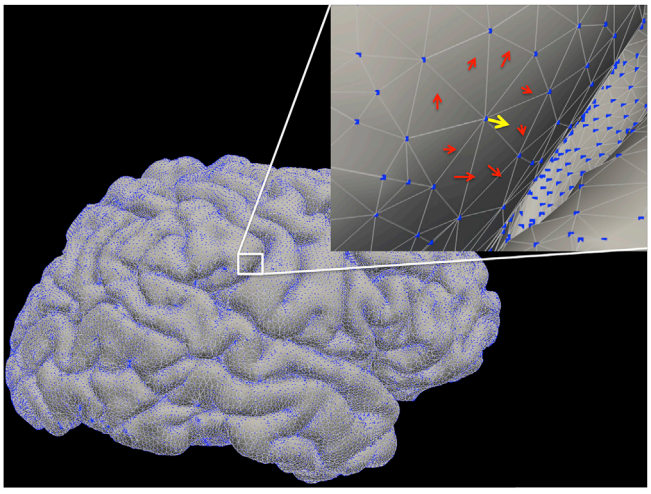

Fig. 3. Surface mesh for an exemplary subject with a schematic representation of a vertex normal. The surface mesh consists of faces (defined by the grey lines) and vertices (blue dots). The normal vector of a vertex (yellow arrow) is approximated by the area-weighted average of the normal vectors (red arrows) of each touching face.

to reduce temporally uncorrelated thermal noise, which is expected to dominate this acquisition given the millimetre-scale voxel size (Triantafyllou et al., 2005) and use of parallel imaging acceleration (Wald and Polimeni, 2017). Exemplar tSNR maps of the 7T fMRI data before and after temporal smoothing are presented in the Supplementary Fig. S1. No spatial smoothing was applied. Finally we calculated each voxel's temporal coefficient of variation, defined as the temporal standard deviation over the mean, or σ/μ (inverse tSNR), as a measure of rs-fMRI signal fluctuation amplitude normalised by the local image intensity.

3.2.4. Registration of surfaces to functional volume and cortical orientation assignment to fMRI data

A rigid (6 degree-of-freedom) registration between each EPI run and the T_1-w data was calculated using FreeSurfer's bbregister (Greve and Fischl, 2009) using the same EPI frame that was used as the reference frame for motion correction. The EPI to T_1-w registration was inverted and applied to all 20 surface meshes to transform them into each subject's EPI space. This operation guarantees that the surface normal orientations computed from the surface meshes will correspond to the head position at the time each EPI run was acquired to account for subject head movement between the T_1-w scan and the EPI runs. The direction cosines of the EPI volume in scanner coordinates were extracted from the data header, then the angles θ_{axis} of each vertex normal to the B_0, PE, RO, and SS axes were calculated as $\theta_{\text{axis}} = \text{acos}(\vec{n} \cdot \vec{e}_{\text{axis}})$, where $\vec{n}$ represents the normal of the vertex and $\vec{e}_{\text{axis}}$ the axis of interest. Finally we wrapped angles from 0° to 180° into orientations 0 to 90° because the orientation effect is symmetric and expected to not depend on the polarity of the surface normal, e.g., the angles +90° and −90° are expected to yield equivalent effects. To confirm proper calculation of the surface orientations, we utilised an anatomical "localiser" scan acquired at the beginning of each session which included a sagittal image exactly parallel to the scanner coordinates as a reference used to verify the direction of the B_0 axis. This axis could be visualised together with the computed surface orientations to confirm their accuracy; an example for surface orientations relative to the B_0 direction is shown in Fig. 2. When applicable, the vessel orientations ϑ_{axis} are defined similarly.

The cortical depth of the EPI voxels were calculated following a "voxel-based approach" as previously described by Polimeni et al. (2018). Cortical depth here is defined as the position of the voxel centroid between the white surface and the pial surface normalised by the local cortical thickness, and therefore ranges in value between 0 and 1. As a convention, the pial surface is defined as depth 1 and the white matter surface is defined as depth 0, a pictorial representation of the depth convention can be found in Fig. 1. As such, the surface at half the cortical grey matter thickness is at depth 0.5, and we refer to this as the "mid-grey surface". Surfaces below the white surface were assigned a negative depth < 0 and we refer to these as "sub-cortical surfaces" in contrast to the intra-cortical surfaces lying at depths between 0 and 1. When defining cortical depths for voxels within the white matter, it is likely that in some white matter voxels there may be multiple possible definitions of cortical depth corresponding to multiple nearby locations in the cortical grey matter. Here, we only consider the depth corresponding to the closest grey matter location. Finally, each voxel is then assigned the quadruple of orientations $[\theta_{B_0}, \theta_{\text{PE}}, \theta_{\text{RO}}, \theta_{\text{SS}}]$ of the surface vertex from the total of 20 surfaces closest in terms of 3D Euclidean distance to the voxel centroid.

There was no B_0 fieldmap acquired for the 7T data. Thus as an alternative strategy, to address potential geometric mismatch of the MEMPRAGE and EPI data biasing the registration, a surface label was created in FreeSurfer to avoid regions that are known to suffer from geometric distortions due to macroscopic susceptibility gradients arising near air-tissue interfaces such as the nasal cavity, ear canals and parts of the orbitofrontal cortex (Greve and Fischl, 2009).

3.3. Analysis

The data were organised in two ways to evaluate the rs-fMRI signal fluctuation amplitudes. The aim was to plot the coefficient of variation, σ/μ, as a function of orientation for a fixed cortical depth and alternatively to plot the data as a function of cortical depth for a fixed orientation. For the former we sorted voxels into relative depth ranges. These were binned by depth between −1.1 to 1.2 with 0.2 spacing. The 3T data were sorted into a depth range between −0.6 and 1.2 with 0.3 spacing because the larger voxel size used at 3T did not provide enough counts at lower depths. Within each depth, voxels were sorted into orientation bins of 5° increments, and σ/μ was then averaged within each bin. The bin centred at $\theta = 87.5°$ with range ±2.5° served as the reference value for normalisation, and so the fluctuation amplitude for voxels within this orientation bin was set to 100% because the BOLD effect should be minimised ($\sin(90°)=0$). The lowest slices were consistently excluded from the analysis due to the strong signal and SNR drop-off towards the neck. To avoid severely distorted areas in the 7T data we excluded voxels that were assigned a vertex within the distortion label (described above) from the analysis.

To calculate cortical depth profiles for voxels at given cortical orientations, we alternatively sorted the voxels into their respective orientation ranges from 0° to 90° in 15° increments. Subsequently voxels were sorted within each orientation range into depth bins of 0.2 relative width, and σ/μ was then averaged bin-wise. Here, the pial surface (depth = 1) served as the reference value for normalisation, and so fluctuation amplitude for voxels within this depth bin was set to 100%.

The largest variation in the BOLD fluctuation amplitude is thought to occur between a parallelly and a perpendicularly oriented cortex. We thus computed the difference in the coefficient of variation between locations where $\theta_{B_0} = 0°$ and where $\theta_{B_0} = 90°$ as the "maximum bias", and calculated this maximum bias as a function of cortical depth.

3.3.1. Signal variance explained as a function of orientation

Nuisance factors other than neuronal activity influence signal fluctuations in the fMRI data. Several of these are expected to generate changes in the susceptibility-induced signal variations (such as the BOLD effect) but also signal variations due to dynamic partial volume effects at tissue boundaries due to motion (bulk and cardio-respiratory induced pulsatility). Therefore we also investigated the orientation bias effects of these nuisance components. To quantify this in the 7T fMRI data, low frequency drift and three physiological noise sources (subject motion, the cardiac and the respiratory cycle) were modelled in a General Linear Model. The drift was modelled as a linear term and subject motion was modelled by the six motion parameter estimates from the motion correction step. The RETROICOR (Glover et al., 2000) method was used to calculate cardiac and respiratory regressors. All regressors were orthogonalized with respect to each other prior to regression to remove shared variance. Note, that for this regression analysis the non-temporally smoothed rs-fMRI timecourses were used. Following the data sorting strategy for orientation and cortical depth described above, we calculated orientation profiles of the variance explained, $R^2(\theta)$, in the 7T data for all four nuisance signal sources as a function of cortical depth.

4. Results

To quantify the distribution of orientations of the cortical surface normal relative to the axes of interest, and identify any potential sampling bias, we computed histograms of the orientations across each imaging slice. Fig. 4 shows the distribution of B_0 and PE orientations over the entire cortex in an exemplar subject. The distributions closely follow the $\sin(\theta)$ curve expected for the uniform sampling distribution of orientations for a sphere, with maximum orientation counts perpendicular (equator) and minimal counts parallel (pole) to the axis. Fig. 4 shows that

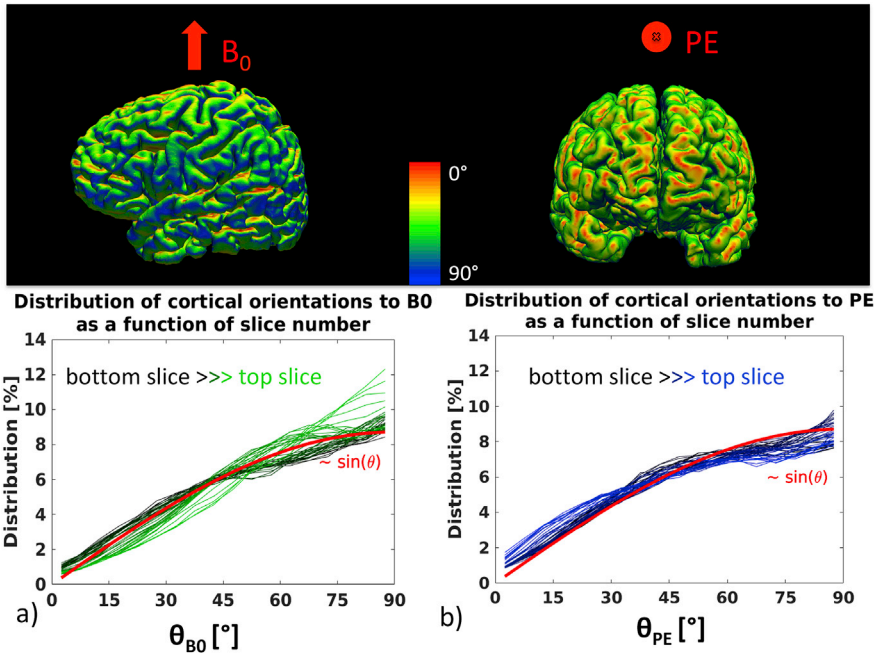

Fig. 4. The distribution of cortical orientations to the B_0 and PE axes for an exemplar subject. The top panel displays the orientations of the cortical surface to B_0 (left, lateral view) and PE (right, anterior view). The bottom panel displays histograms of orientations for each EPI slice. a) The B_0 orientations from the bottom slice (black) to the top slice (green). b) The PE orientations from the bottom slice (black) to the top slice (blue). Both orientations relative to the B_0 and PE axes follow roughly a $\sin(\theta)$ distribution (plotted in red as a reference), which corresponds to the uniform distribution of orientations on a sphere.

the distribution of the cortical surface normal orientations relative to the B_0 axis has an increasing fraction of perpendicular orientations towards the top (higher slice number). This is because most of the human cortex is comprised of sulcal banks. These banks have a surface normal more parallel to B_0 in the middle of the cerebrum and more perpendicular to B_0 towards the top, this can further be appreciated in Fig. 2.

4.1. 7T results

4.1.1. Orientation effects relative to the B_0 axis

Fig. 5 plots the BOLD fluctuation amplitude orientation bias relative to the B_0 axis direction for descending depths, which show that there is a strong *increase* in the BOLD fluctuation amplitudes in cortical regions that are parallel to the B_0 axis relative to regions that are perpendicular to the B_0 axis. The σ/μ plots resemble a $\cos^2(\theta_{B_0})$ curve as expected from the extravascular susceptibility field offset (Eq. (3)). However, the point of maximum bias appears to not always fully align with 0° and tends to be at slightly off-parallel orientations, up to about 15° for some depth (e.g. Fig. 5c), suggesting that there may be an opposing effect that stems from orientation-dependent intravascular contributions to the signal and/or from extravascular field offsets created by the intracortical vessels (see Discussion). Values for the maximum difference – the maximum bias – in BOLD fluctuation observed between regions oriented 90° and 0° relative to the B_0 axis are listed for all depths in Table ST1 in the Supplementary Material. From voxels sampling the pial surface (Fig. 5a), the fluctuation

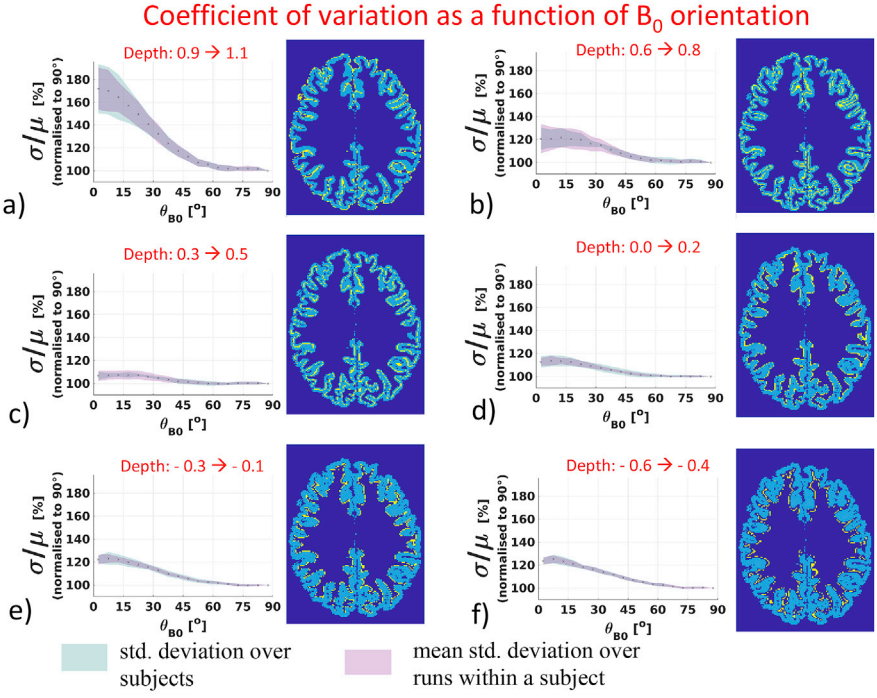

Fig. 5. The dependence of the coefficient of variation, σ/μ, on cortical orientation relative to the B_0 axis, plotted across cortical depths. Each panel (a–f) contains a line plot showing the orientation dependence for one cortical depth. (In each line plot, the green shading represents the standard deviation of the mean across subjects, and the purple shading represents the mean of the standard deviation within a single subject over all EPI runs.). Next to each plot is an exemplar depth mask that indicates the cortical depth sampled in the corresponding line plot (indicated by yellow voxels). BOLD orientation effect from voxels sampling (a) at the pial surface ($0.9 \leq$ depth < 1.1), (b) within the cortex ($0.6 \leq$ depth < 0.8), (c) $0.3 \leq$ depth < 0.5, (d) $0.0 \leq$ depth < 0.2, (e) within the white matter just beneath the grey-white interface ($-0.3 \leq$ depth < -0.1), (f) $-0.6 \leq$ depth < -0.4.

amplitude σ/μ in regions with a surface normal parallel to B_0 exhibits a $+71 \pm 23\%$ increase relative to the fluctuation amplitude observed in regions with a perpendicular orientation. This bias decreases with cortical depth but never fully vanishes, with the smallest bias, $+6 \pm 3\%$, observed at the depth of 0.2 (Fig. 5d). The orientation bias reaches a second maximum of $+25 \pm 4\%$ from voxels sampling within the white matter at a depth of -0.5 (i.e. at a distance of half the cortical thickness below the grey-white boundary, see Fig. 5f).

The cortical depth profiles of the BOLD fluctuation amplitudes, σ/μ, vary with the orientation of the cortex relative to the B_0 axis as shown in Fig. 6a. Here each cortical depth profile corresponds to the BOLD fluctuation amplitudes for voxels within a given orientation bin, and seven depth profiles corresponding to the seven orientation ranges between $[0^\circ, 15^\circ, \ldots, 90^\circ]$ are plotted. Here, curves are normalised to the amplitude at the pial surface as we examine the BOLD fluctuation amplitude depth profile within a fixed orientation bin. As expected, the fluctuation amplitude decreases from the pial surface towards the white matter, but increases again below the grey-white boundary. Depth profiles for different orientation bins differ in their profile gradient. The steepest variation in the BOLD fluctuation amplitudes across cortical depths is found in regions that are oriented parallel to B_0, and the shallowest variation is found in regions that are oriented perpendicular to B_0. This is in line with the assumption that when the cortical surface normal is parallel to B_0 the pial veins are in perpendicular alignment to the B_0 field and maximise their BOLD contribution enhancing the depth profile gradient; whereas the pial veins minimise their contribution to the BOLD signal when the cortical surface normal is perpendicular to B_0. As a control we plotted the BOLD fluctuation amplitude depth profiles as a function of the orientation relative to the RO axis in Fig. 6b. Here, the orientation effect is absent, with no significant effect observed at any cortical depth, as expected.

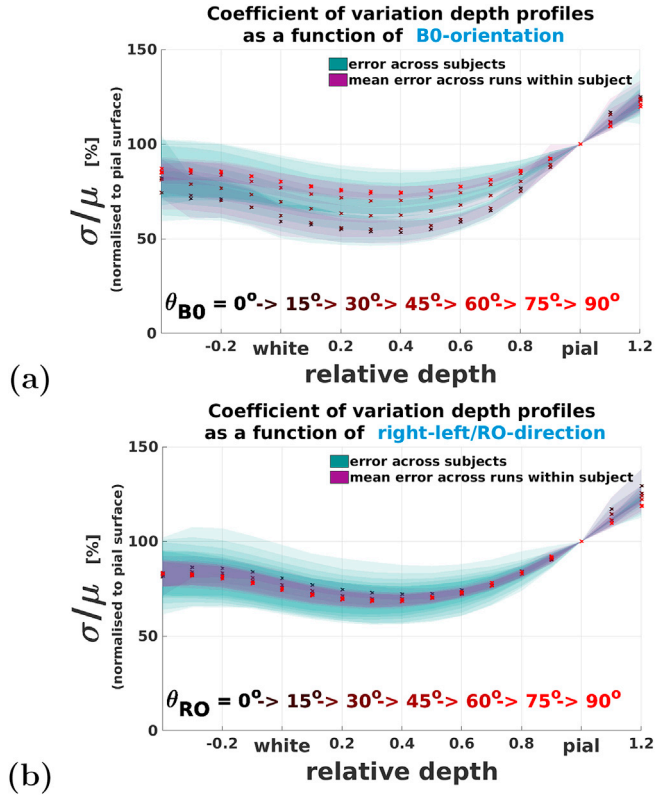

Fig. 6. Cortical depth profile of BOLD fluctuation amplitudes (quantified as σ/μ) for different orientations. Each curve represents the depth profile for voxels within a given orientation bin; the orientation is indicated by the marker color (color scale from black representing 0° to red representing 90°). The blue region surrounding each profile represents the standard deviation across subjects, and the purple region represents the standard deviation across runs within each subject averaged over all subjects. (a) Depth profiles for different orientations relative to B_0: the profile is steepest for cortical regions that are oriented parallel to the direction of B_0 (because for $\theta_{B_0} = 0^\circ$ we go from maximal pial effect to lowest intracortical effect), and flattest for cortical regions that are oriented perpendicular to B_0 (because for $\theta_{B_0} = 90^\circ$ we go from lowest pial effect to maximal intracortical effect), resulting in a spread of cortical depth profiles across orientations that is indicative of an orientation effect. (b) Depth profiles for different orientations relative to the RO axis: profiles are independent of orientation and there is no orientation bias detected along this direction.

4.1.2. *Orientation effects along the anterior-posterior/PE axis*

The BOLD fluctuation amplitude orientation bias with respect to the PE axis direction is plotted for all cortical depths in Fig. 7a–f. The trend seen in the BOLD fluctuation amplitudes as a function of the cortical orientation relative to the PE axis is in the opposite direction compared to the trends seen relative to the B_0 axis: there is a *decrease* in the BOLD fluctuation amplitudes in cortical regions that are parallel to the PE axis compared to regions that are perpendicular to the PE axis, with an observed bias of $-30 \pm 6\%$ between parallel and perpendicular orientation at the pial surface. This bias decreases with cortical depth down to negligible values ($\leq 1\%$) at depths between 0.5 and 0.2. The bias then increases again towards and beyond the grey-white interface with a second maximum bias for voxels within the white matter of $-14 \pm 1\%$ at a depth of -0.4 (i.e. voxels below the white matter surface at a distance of 40% of the cortical thickness). The BOLD fluctuation amplitude depth profile is steepest for cortical orientations that are perpendicular to the PE axis and almost flat for cortical orientations that are parallel to the PE axis; see Fig. 8. The maximum bias values between parallel and perpendicular orientations are listed in Table ST1 in the Supplementary Material.

Non-BOLD sources in our T_2^*-weighted data, such as T_2^*-blurring and voxel displacement due to mesoscopic susceptibility gradients between the grey matter and surrounding CSF including pial surface vessels and white matter, could potentially introduce orientation biases. These additional candidate sources of orientation bias occur along the PE axis direction and we estimated their potential orientation bias (see Supplementary Materials for details). We found the maximum signal biases arising from T_2^*-blurring and voxel displacement due to geometric distortion are each at most below 10%. Thus, we conclude that those effects cannot sufficiently explain the magnitude of the orientation bias along the PE axis observed in our data. To test experimentally that the observed bias along the anterior-posterior/PE direction is not inherent to the choice of the PE axis we rotated the PE direction in a 3T control data set to run from the default anterior-posterior anatomical axis to the right-left anatomical axis. The maximum bias between cortical orientations parallel to versus perpendicular to the PE axis is plotted in Fig. 9 for both the anterior-posterior PE acquisition and the right-left PE acquisition. It can be seen that the maximum bias along the right-left direction is nearly zero for both acquisitions, independent of whether the right-left axis corresponds to the PE direction; whereas a negative bias is observed along the anterior-posterior axis for both acquisitions. We conclude that the negative bias is not due to EPI artefacts along the PE direction such as blurring or distortion and likely solely associated with the projection of the B_0 effect onto the anterior-posterior anatomical axis of the subject (see Discussion).

4.1.3. *Orientation effects in sagittally-acquired control dataset*

A control dataset was acquired with a sagittal slice orientation to test whether the B_0 orientation effect seen in the axially acquired data was simply due to e.g. imperfect slice profiles along the SS direction. The orientation bias with respect to the B_0 axis in the sagittal data set was persistent with about 74% bias at the pial surface between parallel and perpendicular alignment of the cortical surface normal to B_0 (data not shown), which is comparable in magnitude to the axially-acquired data. The cortical depth profiles from this acquisition are shown in Fig. 10. In

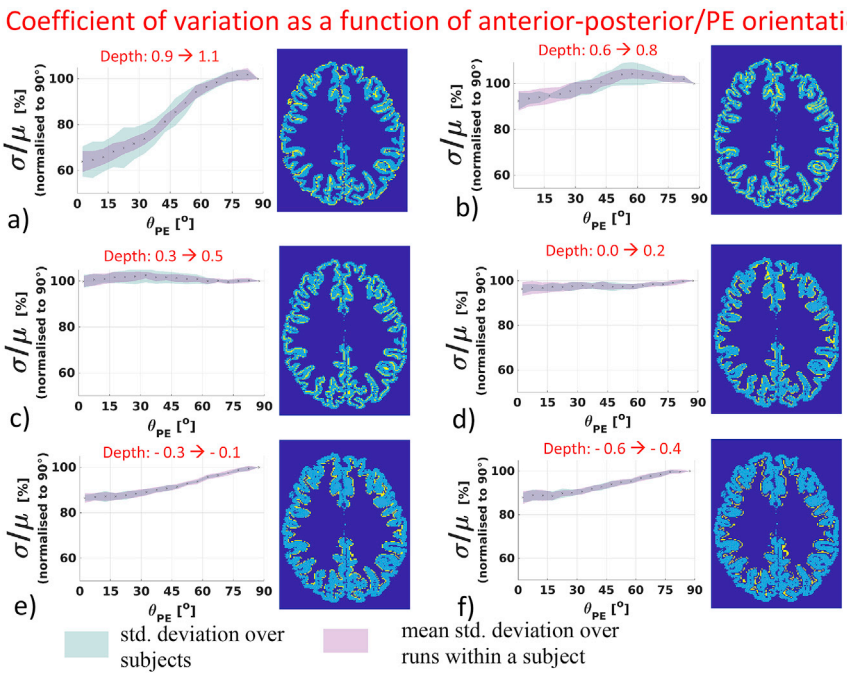

Fig. 7. The dependence of the coefficient of variation, σ/μ, on cortical orientation relative to the PE axis, plotted across cortical depths. Each panel (a–f) contains a line plot showing the orientation dependence for one cortical depth. (In each line plot, the green shading represents the standard deviation of the mean across subjects, and the purple shading represents the mean of the standard deviation within a single subject over all EPI runs.). Next to each plot is an exemplar depth mask that indicates the cortical depth sampled in the corresponding line plot (indicated by yellow voxels). BOLD orientation effect from voxels sampling (a) at the pial surface ($0.9 \leq$ depth < 1.1), (b) within the cortex ($0.6 \leq$ depth < 0.8), (c) $0.3 \leq$ depth < 0.5, (d) $0.0 \leq$ depth < 0.2, (e) within the white matter just beneath the grey-white interface ($-0.3 \leq$ depth < -0.1), (f) $-0.6 \leq$ depth < -0.4.

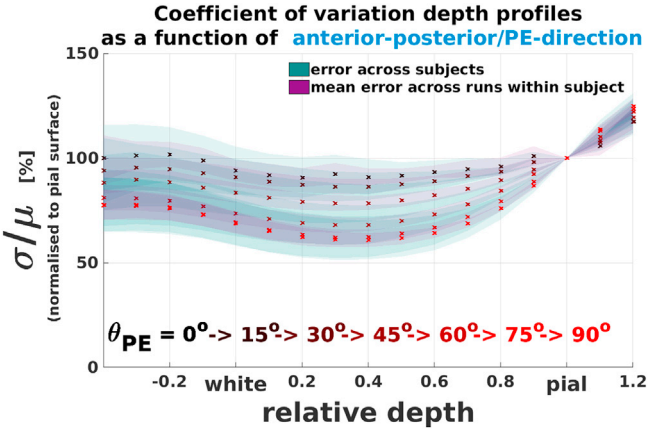

Fig. 8. Cortical depth profile of BOLD fluctuation amplitudes, σ/μ, as a function of orientation relative to the PE axis. Each curve represents the depth profile for voxels within a given orientation bin; the orientation is indicated by the marker color (color scale from black representing 0° to red representing 90°). The blue region surrounding each profile represents the standard deviation across subjects, and the purple region represents the standard deviation across runs within each subject averaged over all subjects. The profile is almost entirely flat for parallel alignment with the PE axis and steepest for perpendicular alignment.

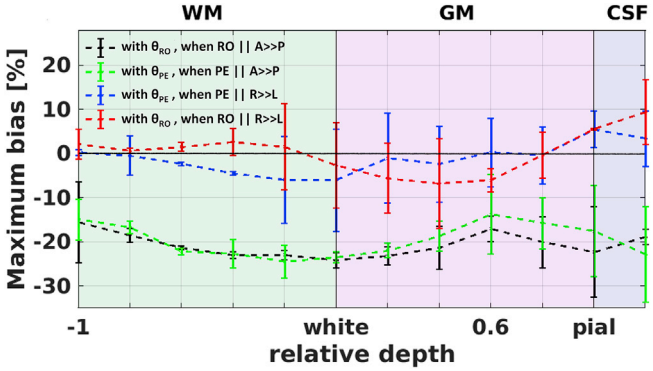

Fig. 9. The maximum bias plotted as a function of cortical depth for two axial acquisitions with either the PE direction set to the default anterior-posterior anatomical axis or to the right-left anatomical axis, plotted for orientation biases relative to the PE axis or to the RO axis. (The light green background indicates depths within white matter, the pink background indicates depths with grey matter, and the light blue background indicates depths within CSF.) Green and blue dotted lines correspond to the orientation bias relative to the PE axis, and black and red dotted lines relative to the RO axis. For both acquisitions a negative bias can be seen relative to the anterior-posterior axis, regardless of the PE direction used for the acquisition, whereas the bias relative to the right-left axis is nearly zero. The error bars represent the standard deviation of the measured bias over the brain.

this case there is no observable orientation effect along the SS axis (now congruent to the right-left anatomical axis), as can be seen in Fig. 10d, whereas the orientation effect relative to the RO axis direction, now closely aligned to the B_0 direction, replicates the behaviour seen in Fig. 6 in which each orientation bin has a distinct depth profile, as can be seen in the spreading of the depth profiles in both Fig. 10a and b. This confirms that there is a strong bias that is a function of the orientation of the cortex relative to the B_0 axis direction and there is no discernible bias that is a function of the orientation relative to the SS axis direction.

4.1.4. *Nuisance variance explained as a function of orientation*

To better understand the source of the orientation bias, we examined whether several individual components of the rs-fMRI signal exhibited an orientation bias relative to axes of interest. Fig. 11 displays the percentage of variance explained, quantified as the R^2 value computed from the linear Pearson correlation coefficient R, for various nuisance components of the signal as a function of the cortical surface orientation relative to the B_0 axis as a function of cortical depth (the same plots relative to the PE axis direction are provided in the Supplementary Fig. S2). The nuisance components examined were those related to low frequency drift, subject motion, and both respiratory and cardiac cycles. The detailed values of the percentage of signal variance explained for all regressors are provided in Table 1 and a summary of the contributions is provided in the Supplementary Fig. S3.

The total percentage of variance explained across all regressors was found to vary with orientation. The largest total signal variance is

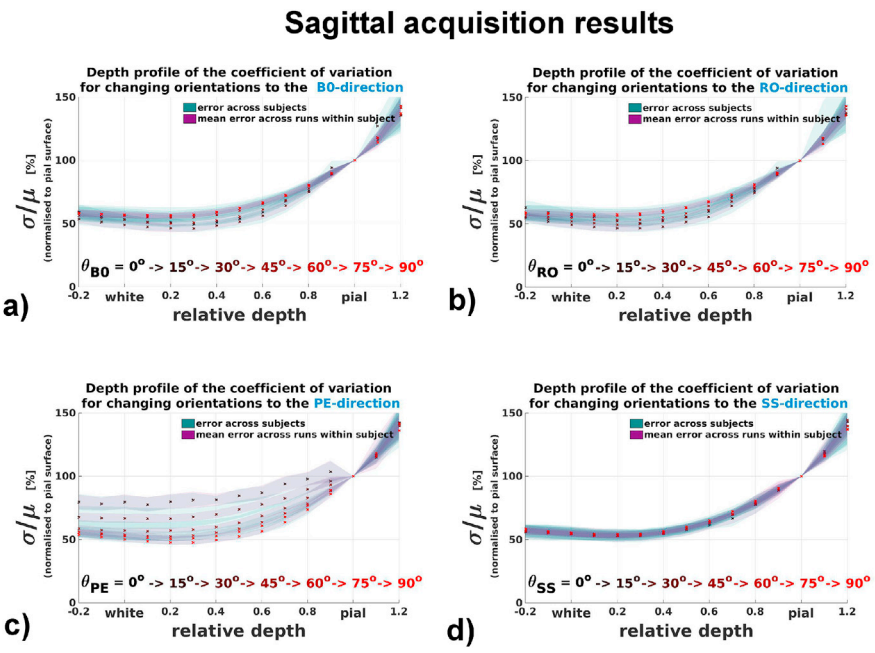

Fig. 10. Cortical depth profiles for the sagittally-acquired EPI data. (a) The BOLD fluctuation amplitudes plotted as a function of cortical depth for each orientation bin individually with respect to the B_0 axis. A clear orientation bias can be seen by the spreading of the cortical depth profiles across the seven orientation bins. (b) The same BOLD fluctuation amplitude depth profiles plotted for various orientations relative to the RO axis, which for this sagittally-acquired dataset is almost perfectly aligned to the B_0 axis. (c) The BOLD fluctuation amplitude plots with respect to the PE axis. As for the axial acquisition results in Fig. 8, there is an orientation bias with respect to the PE axis, which in both this dataset and in the axially-acquired dataset is congruent with the anterior-posterior anatomical axis. (d) The cortical depth profiles across orientation bins relative to the SS axis (that for this dataset is congruent with the right-left anatomical axis) where no orientation effect is seen.

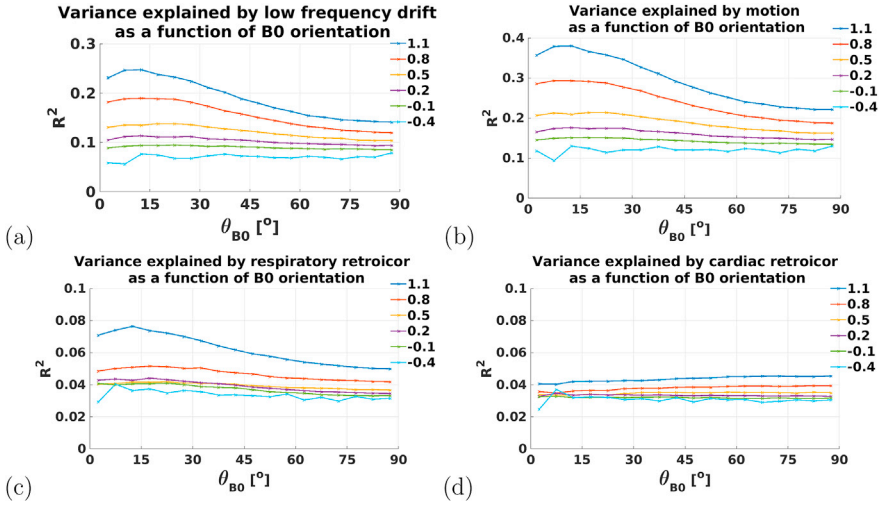

Fig. 11. The percentage of variance explained, R^2, by (a) drift, (b) subject motion, (c) the respiratory cycle, and (d) the cardiac cycle, each as a function of the cortical surface orientation relative to the B_0 axis, plotted across cortical depths. Depths are color-coded from above the pial surface (depth = 1.1) to below the white surface (depth = − 0.4).

explained in regions which are parallel to B_0 and the smallest is explained in regions which are perpendicular to B_0. For example, R^2 is maximised at the pial surface for $\theta_{B_0} = 0°$ with 68% of the rs-fMRI signal variance being explained by drift, motion and physiological sources, whereas for $\theta_{B_0} = 90°$ only 43% of the rs-fMRI signal variance is explained.

The component that explained the largest amount of the signal variance was motion. Here, we present the R^2 values as a measure of percentage of variance explained for all six motion parameters combined. Individual plots for the three rotations (pitch, roll and yaw) and the three translations (*x*,*y*,*z*) can be found in Supplementary Figs. S4 and S5 respectively. R^2 was similar for all three rotation parameters and the translation parameters along the scanner's *x* and *y* axes. However, R^2 was slightly larger along the z direction, which is likely due to spin-history effects along the SS direction which is closely aligned with the *z* axis in an axial acquisition.

Motion induces signal variance that is dependent on the orientation of the cortical surface normal, as cortical locations with a surface normal that is aligned parallel to B_0 moves pial vessels that are perpendicular to B_0 and exhibit a maximum signal, compared to cortical locations where the surface normal is perpendicular and pial vessels are parallel to B_0 and thus invisible. However, additionally motion causes partial volume fluctuations in the voxel and we estimated the maximal orientation bias that could arise from the exchange of grey matter (that has an orientation-dependent T_2^* (Cohen-Adad et al., 2012)) and CSF (that has an orientation-*independent* T_2^*) and found this to be at most an order of magnitude smaller than the orientation bias magnitude observed in the data (see Supplementary Material 1 for details).

As motion is the largest explanatory variable here, we further tested if subjects that moved more during the scans exhibit an overall higher orientation bias magnitude $\left(\frac{\sigma}{\mu}(\theta_{B_0} = 90°) - \frac{\sigma}{\mu}(\theta_{B_0} = 0°)\right)$. There was no correlation between the latter and the subjects' total absolute translation and rotation ($p = 0.58$ and $p = 0.65$) as well as the standard deviation of relative translation and rotation ($p = 0.75$ and $p = 0.54$), measured at the

Table 1
Percentage of variance explained, R^2, of the rs-fMRI signal as a function of the cortical surface orientation relative to the directions of the B_0 and PE axes, from voxels sampling from the pial, mid-grey, and white matter surfaces. The corresponding pie charts can be found in the Supplementary Fig. S3. The total variance explained is highlighted and is the sum of the variance from all individual regressors.

Relative cortical depth ±0.1	Source	Percentage of variance explained, R^2			
		$\theta_{B_0} = 0°$	$\theta_{B_0} = 90°$	$\theta_{PE} = 0°$	$\theta_{PE} = 90°$
pial	Low frequency drift	0.23 ± 0.03	0.13 ± 0.02	0.12 ± 0.02	0.17 ± 0.02
	Subject motion	0.35 ± 0.04	0.21 ± 0.02	0.20 ± 0.02	0.26 ± 0.03
	Cardiac	0.04 ± 0.01	0.04 ± 0.01	0.04 ± 0.01	0.04 ± 0.01
	Respiration	0.06 ± 0.01	0.05 ± 0.01	0.05 ± 0.01	0.05 ± 0.01
	total	0.68	0.43	0.41	0.53
mid-grey	Low frequency drift	0.13 ± 0.02	0.10 ± 0.02	0.11 ± 0.02	0.11 ± 0.02
	Subject motion	0.21 ± 0.03	0.16 ± 0.02	0.17 ± 0.02	0.18 ± 0.02
	Cardiac	0.03 ± 0.01	0.04 ± 0.01	0.04 ± 0.01	0.03 ± 0.01
	Respiration	0.04 ± 0.01	0.04 ± 0.01	0.04 ± 0.01	0.04 ± 0.01
	total	0.41	0.34	0.35	0.36
white matter	Low frequency drift	0.10 ± 0.02	0.09 ± 0.01	0.09 ± 0.02	0.09 ± 0.02
	Subject motion	0.16 ± 0.02	0.14 ± 0.01	0.14 ± 0.02	0.14 ± 0.02
	Cardiac	0.03 ± 0.01	0.03 ± 0.01	0.03 ± 0.01	0.03 ± 0.01
	Respiration	0.04 ± 0.01	0.03 ± 0.003	0.04 ± 0.01	0.04 ± 0.01
	total	0.33	0.29	0.29	0.30

pial surface (depth = 1.0).

The second largest R^2 was observed for low frequency drift, followed by respiration, and the smallest contribution is the signal component related to the cardiac cycle. The orientation bias declines but remains non-zero throughout all cortical depths for all regressors except for the cardiac regressor, which is the only component that appears to be independent of orientation. Because the orientation effect is caused by the angular dependence of the vascular field offset due to susceptibility effects, only those components of the time-series signal that are driven by susceptibility changes are expected to exhibit an orientation effect; therefore we interpret the lack of a detectable orientation effect with the cardiac component as evidence that time-series signal fluctuations in our data that are correlated with the cardiac cycle are not primarily caused by changes in susceptibility, but rather are more likely due to dynamic partial volume effects (see Discussion).

The two columns furthest to the right in Table 1 summarises the percentage of variance explained, R^2, as a function of PE orientation, θ_{PE}, and cortical depth (see also Supplementary Figs. S2 and S3). Here, the total physiological noise contribution is maximised for cortical regions that are perpendicular to the PE axis direction (i.e. $\theta_{PE} = 90°$) with $R^2 = 0.53$ at the pial surface. Within the cortex at the mid-grey depth, the percentage of variance explained loses its orientation dependence, and $R^2 = 0.35$ at $\theta_{PE} = 0°$ and $R^2 = 0.36$ at $\theta_{PE} = 90°$. As with the B_0 axis, the cardiac regressor is independent of orientation to the PE axis. The similar lack of orientation dependence for the cardiac regressor along the B_0 and the anterior-posterior direction suggest that the latter bias might be a projection of the former.

4.2. 3T results

Susceptibility effects increase with field strength and resolution, so we tested whether similar orientation effects could be observed in rs-fMRI data at the more conventional field strength of 3T and 2 mm isotropic resolution. Orientation effects were also detectable, however were observed to be of smaller magnitude compared to the high-resolution 7T data. The maximum bias values across all cortical depths and for all axes are listed in Table ST2 in the Supplementary Material. The maximum orientation bias with respect to the B_0 axis is detected below the white surface at a relative depth of −0.4 with $+16 \pm 7\%$; this maximal bias was higher than the bias found at the pial surface, which exhibited a maximum bias of $11 \pm 12\%$. The bias with respect to the PE axis is of comparable magnitude to the bias with respect to the B_0 axis, with a maximum bias at the pial surface of $-13 \pm 7\%$.

4.3. Summary of orientation bias quantified both at 7T and 3T

Fig. 12 summarises the maximum orientation bias found in the BOLD fluctuation amplitudes between regions where the cortical orientation was perpendicular to and parallel to the direction of either the B_0 or PE axes for the 1.1 mm 7T and 2 mm 3T axially-acquired data. The B_0 orientation effect is more than 6 times larger at the pial surface in the 7T data than in the 3T data, whereas the bias is comparable between 7T and 3T from the mid-grey depth to the white matter surface; beneath the grey-white interface, the trends in the 7T and 3T datasets diverge again, with the 7T data exhibiting a bias level that is twice that of the 3T data. For the bias relative to the PE axis, the 7T data exhibit a bias that is about twice that of the 3T data from voxels sampling the pial surface, however the biases in the 7T and 3T data are comparable in magnitude for all other cortical depths.

5. Discussion

Here, we demonstrated B_0 orientation biases in rs-fMRI data across all cortical depths. These biases nearly follow the predicted $\cos^2(\theta_{B_0})$ dependence of the gradient-echo BOLD signal change with cortical orientation θ_{B_0} expressed in Eq. (3) as expected for when contributions from pial vessels dominate, reflecting the expected $\sin^2(\vartheta_{B_0,\text{vessel}})$ dependence of extravascular susceptibility field offsets on vessel orientation $\vartheta_{B_0,\text{vessel}}$ expressed in Eq. (2). This bias was substantially more pronounced in the 1.1 mm 7T data, compared to the 2 mm 3T data, which reflects both an increase in the effect with higher field strength and, potentially, an increase in the effect with decreasing voxel size, thus partial volumes.

It should also be noted that the TE of 29 ms used in the 3T acquisition is below the T_2^* of deoxygenated venous blood (assuming an oxygen saturation of venous blood of 60%) at 3T (approximately 35 ms). Hence, based on our acquisition parameters, the 3T BOLD signal in our data should be more weighted towards intravascular field offsets, compared to

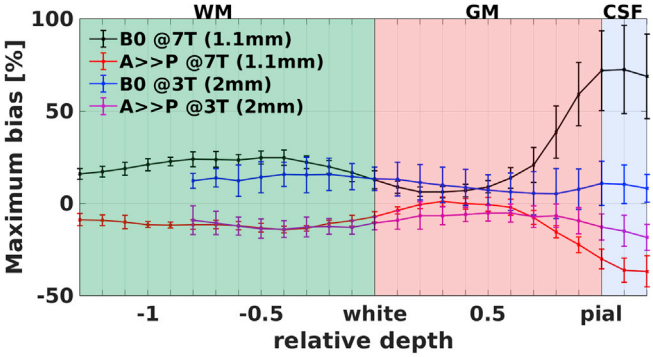

Fig. 12. A summary of the maximum bias found in the BOLD fluctuation amplitudes between regions where the cortical orientation was perpendicular to and parallel to the direction of either the B_0 or anterior-posterior/PE axes for the 1.1 mm 7T and 2 mm 3T axially-acquired data. The black and blue lines present the B_0 bias at 7T and 3T; the red and pink lines the anterior-posterior/PE bias respectively. The error bars indicate the standard deviation across all subjects. For the 7T data the B_0 bias between perpendicular and parallel orientation is maximised at and above the pial surface (blue shade) and drops of towards cortical mid-grey (pink shade) and reaches a second local maximum in the white matter (green shade). The 3T data shows a smaller amplitude of the effect but follows a similar trend. The anterior-posterior/PE bias is similarly maximised at the pial surface, drops towards zero towards and beyond the mid-grey depth and increases again in the white matter.

our 7T data. At 7T the TE is usually chosen to maximise tissue functional CNR, here we chose 25 ms, which is somewhat longer than the venous blood T_2^* value at 7T which reduces the contribution of intravascular field components. Hence, the differences in our 3T and 7T data in the ratio of intravascular versus extravascular signal levels is likely somewhat enhanced due to our choices of TE values.

The maximum bias of the BOLD fluctuation amplitudes, quantified using the temporal coefficient of variation, σ/μ, was detected for voxels sampling at the pial surface at about +71% at 7T. We hypothesized that the rs-fMRI amplitude would be maximised for cortical locations that were parallel to the B_0 axis, as this is the configuration where all of the large pial veins are perpendicular to B_0 and thus maximise their extravascular field component. However, we found that the maximum amplitude did not consistently occur at $\theta_{B_0} = 0^\circ$ exactly, but was slightly offset by a few degrees at some depths, e.g. depth = 0.4 (Fig. 5c). This could be related to a counter-acting intravascular field component, that follows an orthogonal $\cos^2(\vartheta_{B_0,\text{vessel}})$ susceptibility effect and for pial vessels would manifest as a $\sin^2(\theta_{B_0})$ effect relative to the cortical orientation, as expressed in Eqs. (1) and (4). Also in support of a significant intravascular BOLD contribution is that this peak offset was enhanced at 3T (data not shown) where the maximum was shifted to larger angles ($\approx 25^\circ$) and the minimum to even smaller angles ($\approx 75^\circ$) than at 7T. This is expected at 3T where the intravascular component is more dominant. It could also be related to extravascular contribution of the intracortical vessels, which are oriented perpendicular to pial vessels and counteract their effect.

Although the bias decreased for grey matter voxels sampling progressively further from the pial surface towards cortical mid-grey, it unexpectedly but consistently increased again towards and beyond the grey-white interface and into the white matter.

5.1. Increased B_0 orientation bias at the white matter surface: effects of "principal vessels"?

The secondary peak in the depth profiles of the bias—about +25% at 7T and at +16% at 3T—is observed within the white matter at a distance of roughly half the cortical thickness from the white matter surface. This suggests that there is a BOLD effect within the white matter from a vascular feature similar to the vasculature found on the pial surface, e.g., a similar vascular network lying just beneath the grey-white interface. These white matter vessels have indeed been observed by Duvernoy et al. (1981), who named them "principal vessels", and by several others (Pfeifer, 1928; Hirsch et al., 2013). These vessels pass perpendicular through the cortex into the white matter in a radial fashion, then bend and run approximately towards the brain centre, i.e. at the flat banks of sulci they tend to bend at nearly right angles as soon as they enter into the white matter and then run tangential to the grey-white interface, as can been readily seen in the classic report of Duvernoy et al. (1981). Hernández-Torres et al. (2017) and Doucette et al. (2019) recently reported a dependence in cerebral blood volume and flow measurements on white matter fibre tract orientation in dynamic susceptibility contrast imaging. They relate this orientation dependence to vessels running parallel to the white matter fibre tracts. The orientation dependence in our BOLD EPI data is likely an equivalent to their observations as white matter fibres tend to run radially towards the middle of the brain and thus parallel to the cortical banks.

It is currently unclear whether the BOLD signal detected from these vessels within the white matter reflects drained deoxygenated blood from deep grey matter nuclei or from fibre bundles within the white matter. There have been observations of BOLD signal changes within the white matter (Gawryluk et al., 2014; Peer et al., 2017; Ding et al., 2017; Özbay et al., 2018), and therefore the signal changes within these subjacent vessels is a worthy topic for further investigation. Nevertheless, because the BOLD signal mainly reflects changes in deoxyhaemoglobin concentration, it is primary a venous signal, and since these white matter veins exit the white matter by passing through the grey matter and are in turn drained by the large pial vessels, BOLD signal changes from these white matter vessels are not expected to reflect neuronal activity from the cortical grey matter, however they will still likely reflect systemic physiological fluctuations commonly seen within the white matter (Özbay et al., 2018).

5.2. Orientation effects relative to the anterior-posterior axis

The BOLD fluctuation amplitudes were further influenced by the cortical orientation relative to the anterior-posterior axis, with a decrease in σ/μ found in regions where the cortex was oriented parallel to this anatomical axis. The bias was again maximised at the pial surface and, in contrast to the B_0 orientation effect, became negligible at the mid-grey depth. This observation was consistent across the 3T and 7T data sets: the anterior-posterior bias re-emerged near to and beyond the grey-white interface. Because in our primary dataset the anterior-posterior direction was aligned with the EPI PE direction, a simple explanation for the observed bias could have been T_2^*-blurring and geometric distortion along the PE direction, causing a reduction in BOLD fluctuation amplitude; however, this is not the case—when the PE and RO directions were exchanged by rotating the axial slices, an orientation bias relative to the anterior-posterior axis remained. This suggests that it is a projection of the B_0 effect (a location that is parallel to B_0 will always be perpendicular to the anterior-posterior axis etc.) and that this projection is enhanced along the anterior-posterior axis and potentially driven by an anatomical asymmetry. The human brain is commonly more elliptical than circular due to its elongation along the anterior-posterior direction; to rule out that this observed effect is a form of sampling bias we performed a control analysis where angular histograms between right-left and anterior-posterior were matched to equal counts (data not shown), yet the results did not change and the orientation bias remained. An explanation for this orientation bias relative to the anterior-posterior anatomical axis is the topic of ongoing investigations.

5.3. Percentage of variance explained as a function of orientation

The high-resolution 7T data, with a voxel volume of 1.3mm^3, were thermal noise-dominated, as expected (Triantafyllou et al., 2005; Wald and Polimeni, 2017). This can be seen in Supplementary Fig. S1, where the tSNR values in white matter are smaller than in grey matter as expected for thermal noise dominated data. Of the modelled sources of variance, the motion parameters explained the largest share of variance (14–35%). Rotational and translational parameters showed comparable levels of signal variance explained, except for the motion in the $z$direction, which is likely enhanced due to true as well as apparent motion from breathing for oblique axial slices where the PE direction has some component along z (Fair et al., 2018; Chen et al., 2019).

We observed that the amount of variance explained by rigid-body motion was a function of cortical orientation in a way that is consistent with the BOLD fluctuation amplitudes, in that motion explained more variance at locations that were parallel to the B_0 axis, and with more variance explained at the pial surface. This is likely attributable to the motion of cortical vessels with the head during motion, i.e. a vessel that is perpendicular to B_0 will cause a larger change in the BOLD signal when it moves than a vessel that is parallel to B_0. Indeed, there was no correlation between how much a subject moved during an rs-fMRI run and the orientation bias magnitude of that run. We do not expect partial voluming to be the cause of the orientation dependence of the variance explained by motion; and we found that the estimate of the maximum orientation bias that could be induced by dynamic partial voluming is an order of magnitude smaller than the orientation bias values in our data. This suggests that these signal changes due to dynamic partial voluming of the tissue are not likely to be the main cause of our observed orientation bias and it is far more likely to be driven by BOLD changes induced by the vasculature. The second largest explanatory variable is low fre-

quency drift (9–23%), followed by the respiratory cycle (3–6%), and the smallest percentage of signal variance was attributed to the cardiac cycle (3–4%). A similar signal composition has so far been observed in a 7T study by Bianciardi et al. (2009) where 3 mm^3 voxels were dominated by low frequency drift signals whereas cardio-respiratory signals contributed the least. All nuisance regressors showed an orientation dependence, especially in voxels sampling near to the pial surface, with the notable exception of the cardiac regressor. The lack of any orientation effect in the component correlated with the cardiac regressor suggests that the time-series signal fluctuations driven by the cardiac cycle may not be attributable to a susceptibility effect and cardiac pulsatility is thought to mainly affect the arteries that contain fully oxygenated blood (Bianciardi et al., 2016). Signal fluctuations driven by cardiac pulsatility may be more likely due to dynamic partial volume effects, which is in agreement with previous reports on T_2^* fluctuations driven by the cardiac cycle at 7T (Viessmann et al., 2017). One may speculate that for acquisition parameters that specifically enhance the cardiac-driven component the orientation effect may diminish once this component explains a higher share of the time-series variance.

5.4. Potential statistical biases

The large proportion of variance explained by the orientation bias suggests that rs-fMRI derived measures have potential to be biased by the cortical orientations found within a given region of interest. Analysis pipelines often use volume-based smoothing that could help to suppress the effect, and group-level analyses across large populations might act to average out the bias. However, given the brain's strong left-right symmetry, cortical regions across the hemispheres share the same orientation if the subject lies in the scanner in the standard head-first-supine position. A recent 7T fMRI study with half-millimetre voxel size by Fracasso et al. (2018) reported a $\cos^2(\theta_{B_0})$ dependence of the percentage BOLD signal change over the primary visual cortex area (V1) for a visual stimulus task. More investigation is needed to test if orientation effects have a substantial impact more broadly on either task-driven activation or resting-state connectivity measures based on gradient-echo BOLD fMRI. It should also be noted that this orientation bias is based on T_2^* susceptibility effects and should not be present in non-BOLD fMRI that more directly measure changes in cerebral blood volume such as vascular space occupancy (VASO) (Lu et al., 2003; Huber et al., 2015) or cerebral blood flow, such as arterial spin labelling (ASL).

5.5. Critical points and limitations

It should be noted that the orientation distribution across the cortex is not uniform (Fig. 4), but closely follows a $\sin(\theta_{B_0})$ curve. If we consider the normal vector to have unit length, the collection of normal vectors can be parameterized by the unit sphere aligned around an axis of interest. There are only two configurations for the cortical surface normal vector to be aligned to the axis of interest (parallel and anti-parallel), corresponding to vectors directed to either of the two poles of the sphere, but there are far more configurations for the vector to be perpendicular to the axis of interest (i.e. any vector pointing to a point along the equator of the sphere). Because the largest bias will occur for the parallel/anti-parallel orientations, the largest bias corresponds to the orientation that is the least likely to be encountered.

5.6. Towards microvascular-specific fMRI in humans

The effects of cortical orientation at different cortical depths demonstrated in this work emphasize the need for a more detailed account of the vascular content of high-resolution fMRI voxels. Biophysical BOLD signal modelling using anatomically-realistic microvascular anatomy (Gagnon et al., 2015; Boas et al., 2008) may be increasingly mandatory to understand the BOLD signal as imaging resolutions reach the scale where the meso- and micro-scale vasculature changes dramatically between neighbouring voxels. Kennel et al. (2017) theoretically predict variations of up to 500% between parallel and perpendicular orientation for a 500 mm^3 voxel containing vasculature from primate cortex, and the equivalent spatial resolution for whole-brain human fMRI is likely to be achievable within the next years (Polimeni and Wald, 2018).

The observed orientation bias in the data presented in this study was entirely dominated by the pial and white matter vasculature at all cortical depths. The intracortical ascending venules are mid-sized veins that run perpendicularly to the cortical surface and are parallel to the local cortical surface normal. As such they should exhibit a maximal BOLD signal at cortical locations with perpendicular orientation relative to the B_0 axis and minimal BOLD signal locations with a parallel orientation, thus have an opposite effect to that expected for the pial vasculature to which they are orthogonal. However, we do not observe such an inversion of the bias at intra-cortical depths. We conclude that gradient-echo EPI with 1.3 mm^3 volume is dominated by the large pial vessels, and relatively insensitive to the intracortical ascending venules. This dominance of the pial vessel component in our data is likely due to a combination of partial volume effects that can be altered by the acquisition resolution, but also due the large extent of the extravascular field that penetrates into the cortex below the pial surface for larger vessel diameters. This is independent of voxel resolution and, unfortunately, for this reason simply excluding voxels intersecting the pial surface will unlikely eliminate the bias.

5.7. Outlook, orientation bias correction, and quantifying vascular influences on fMRI data

Because BOLD fMRI amplitudes are biased by local cortical orientation, and the effect increases with higher field strength and smaller voxels, this purely vascular bias does impose a challenge to more accurately infer neuronal activity from high-resolution fMRI data. However, this bias is well-characterized and is predictable from the cortical surface geometry, and thus it should be straightforward to account for this bias during data analysis, e.g., via regression against cortical surface orientation. As such it can be regarded as yet another nuisance factor that influences the BOLD fMRI signal. On the other hand, these orientation biases in the BOLD fMRI data offer the possibility to test for vascular specificity of other candidate BOLD fMRI approaches that promise microvascular weighting, such as various forms of spin-echo-based BOLD fMRI—in particular, EPI-based spin-echo BOLD can exhibit varying levels of unwanted large-vessel sensitivity with different acquisition parameter values (Goense and Logothetis, 2006), which would also induce varying levels of orientation dependence. The vascular influences on the BOLD fMRI signal can therefore potentially be quantified by examining how the fMRI signal varies as a function of cortical orientation as well as cortical depth.

5.8. Conclusion

In this study we have demonstrated that resting-state BOLD fMRI fluctuation amplitudes vary systematically with the cortical folding pattern and are influenced by the local cortical orientation relative to the B_0 axis. We demonstrated that these biases vary systematically with cortical depth and that they reflect the anatomy of the cortical vasculature including the well-known pial vasculature on the cortical surface as well as lesser-known vasculature just beneath the grey-white interface. While this bias poses challenges to the interpretation of BOLD fMRI data, it is predictable from the cortical geometry and expected to be straightforward to remove.

Acknowledgements

We thank Dr. Jingyuan Chen for her help with the calculation of the

RETROICOR regressors, Dr. Anna Błażejewska for providing the B_0 geometric distortion label, Mr. Ned Ohringer for help with subject recruitment and scanning, and Prof. David Kleinfeld for helpful discussions regarding the white matter vasculature. We also thank Dr. Anna Błażejewska and Dr. Avery Berman for discussions on non-BOLD signal sources that exhibit orientation effects. This work was supported in part by the NIH NIBIB (grants P41-EB015896, R01-EB023281, and R01-EB019437), by the NEI (R01-EY026881), by the *BRAIN Initiative* (NIMH grants R01-MH111419, R01-MH111438, R24-MH106053, and R24-MH106096 and NIBIB grants U01-EB025162 and U01-EB025121), by the MGH/HST Athinoula A. Martinos Center for Biomedical Imaging, and made possible by NIH NCRR Shared Instrumentation Grants S10-RR023401, S10-RR023043 and S10-RR020948.

Appendix A. Supplementary data

Supplementary data to this article can be found online at https://doi.org/10.1016/j.neuroimage.2019.04.036.

References

Ashburner, J., Barnes, G., Chen, C., Daunizeau, J., Flandin, G., Friston, K., Kiebel, S., Kilner, J., Litvak, V., Moran, R., et al., 2014. SPM12 Manual. Wellcome Trust Centre for Neuroimaging, London, UK.

Báez-Yánez, M.G., Ehses, P., Mirkes, C., Tsai, P.S., Kleinfeld, D., Scheffler, K., 2017. The impact of vessel size, orientation and intravascular contribution on the neurovascular fingerprint of bold bssfp fmri. Neuroimage 163, 13–23.

Bandettini, P.A., Wong, E.C., 1995. Effects of biophysical and physiologic parameters on brain activation-induced R2* and R2 changes: simulations using a deterministic diffusion model. Int. J. Imaging Syst. Technol. 6 (2–3), 133–152.

Bandettini, P.A., Wong, E.C., Hinks, R.S., Tikofsky, R.S., Hyde, J.S., 1992. Time course epi of human brain function during task activation. Magn. Reson. Med. 25 (2), 390–397.

Bender, B., Klose, U., 2010. The in vivo influence of white matter fiber orientation towards B0 on T2* in the human brain. NMR Biomed. 23 (9), 1071–1076.

Bianciardi, M., Fukunaga, M., van Gelderen, P., Horovitz, S.G., de Zwart, J.A., Shmueli, K., Duyn, J.H., 2009. Sources of functional magnetic resonance imaging signal fluctuations in the human brain at rest: a 7T study. Magn. Reson. Imag. 27 (8), 1019–1029.

Bianciardi, M., Toschi, N., Polimeni, J.R., Evans, K.C., Bhat, H., Keil, B., Rosen, B.R., Boas, D.A., Wald, L.L., Bianciardi, M., Toschi, N., Polimeni, R., Evans, K.C., Bhat, H., Keil, B., Rosen, B.R., Boas, D.A., Wald, L.L., 2016. The pulsatility volume index: an indicator of cerebrovascular compliance based on fast magnetic resonance imaging of cardiac and respiratory pulsatility. Phil. Trans. Math. Phys. Eng. Sci. 374 (2067), 20150184.

Boas, D.A., Jones, S.R., Devor, A., Huppert, T.J., Dale, A.M., 2008. A vascular anatomical network model of the spatio-temporal response to brain activation. Neuroimage 40 (3), 1116–1129.

Boxerman, J.L., Hamberg, L.M., Rosen, B.R., Weisskoff, R.M., 1995. MR contrast due to intravascular magnetic-susceptibility perturbations. Magn. Reson. Med. 34 (4), 555–566.

Buxton, R.B., 2009. Introduction to Functional Magnetic Resonance Imaging: Principles and Techniques. Cambridge University Press.

Chen, J.E., Polimeni, J.R., Bollmann, S., Glover, G.H., 2019. On the analysis of rapidly sampled fmri data. Neuroimage 188, 807–820.

Cohen-Adad, J., Polimeni, J.R., Helmer, K.G., Benner, T., McNab, J.A., Wald, L.L., Rosen, B.R., Mainero, C., 2012. T2* mapping and B0 orientation-dependence at 7T reveal cyto- and myeloarchitecture organization of the human cortex. Neuroimage 60 (2), 1006–1014.

Ding, Z., Huang, Y., Bailey, S.K., Gao, Y., Cutting, L.E., Rogers, B.P., Newton, A.T., Gore, J.C., 2018. Detection of synchronous brain activity in white matter tracts at rest and under functional loading. Proc. Natl. Acad. Sci. Unit. States Am. 115 (3), 595–600.

Doucette, J., Wei, L., Hernández-Torres, E., Kames, C., Forkert, N.D., Aamand, R., Lund, T.E., Hansen, B., Rauscher, A., 2019. Rapid solution of the Bloch-Torrey equation in anisotropic tissue: application to dynamic susceptibility contrast MRI of cerebral white matter. Neuroimage 185, 198–207. October 2018.

Duong, T.Q., Yacoub, E., Adriany, G., Hu, X., Ugurbil, K., Kim, S.-G., 2003. Microvascular BOLD contribution at 4 and 7T in the human brain: gradient-echo and spin-echo fMRI with suppression of blood effects. Magn. Reson. Med. 49 (6), 1019–1027.

Duvernoy, H.M., Delon, S., Vannson, J.L., 1981. Cortical blood vessels of the human brain. Brain Res. Bull. 7 (5), 519–579.

Fair, D.A., Miranda-Dominguez, O., Snyder, A.Z., Perrone, A.A., Earl, E.A., Van, A.N., Koller, J.M., Feczko, E., Klein, R.L., Mirro, A.E., Hampton, J.M., Adeyemo, B., Laumann, T.O., Gratton, C., Greene, D.J., Schlaggar, B., Hagler, D., Watts, R., Garavan, H., Barch, D.M., Nigg, J.T., Petersen, S.E., Dale, A., Feldstein-Ewing, S.W., Nagel, B.J., Dosenbach, N.U.F., 2018. Correction of Respiratory Artifacts in MRI Head Motion Estimates. bioRxiv.

Fischl, B., 2012. FreeSurfer. Neuroimage 62 (2), 774–781.

Fracasso, A., Luijten, P.R., Dumoulin, S.O., Petridou, N., 2018. Laminar imaging of positive and negative BOLD in human visual cortex at 7T. Neuroimage 164, 100–111.

Gagnon, L., Sakadžić, S., Lesage, F., Musacchia, J.J., Lefebvre, J., Fang, Q., Yucel, M.A., Evans, K.C., Mandeville, E.T., Cohen-Adad, J., Polimeni, J.R., Yaseen, M., Lo, E.H., Greve, D.N., Buxton, R.B., Dale, M., Devor, A., Boas, D.A., 2015. Quantifying the microvascular origin of BOLD-fMRI from first principles with two-photon microscopy and an oxygen-sensitive nanoprobe. J. Neurosci. 35 (8), 3663–3675.

Gagnon, L., Sakadžić, S., Lesage, F., Pouliot, P., Dale, A.M., Devor, A., Buxton, R.B., Boas, D.A., 2016. Validation and optimization of hypercapnic-calibrated fmri from oxygen-sensitive two-photon microscopy. Philosoph. Trans. Roy. Soc. B 371 (1705), 20150359.

Gawryluk, J.R., Mazerolle, E.L., D'Arcy, R.C.N., 2014. Does functional MRI detect activation in white matter? A review of emerging evidence, issues, and future directions. Front. Neurosci. 8, 239.

Glover, G.H., Li, T.Q., Ress, D., 2000. Image-based method for retrospective correction of physiological motion effects in fMRI: RETROICOR. Magn. Reson. Med. 44 (1), 162–167.

Goense, J.B.M., Logothetis, N.K., 2006. Laminar specificity in monkey V1 using high-resolution SE-fMRI. Magn. Reson. Imag. 24 (4), 381–392.

Greve, D.N., Fischl, B., 2009. Accurate and robust brain image alignment using boundary-based registration. Neuroimage 48 (1), 63–72.

Haacke, E.M., Mittal, S., Wu, Z., Neelavalli, J., Cheng, Y.-C.N., 2009. Susceptibility-weighted imaging: technical aspects and clinical applications, part 1. Am. J. Neuroradiol. 30 (1), 19–30.

Hänninen, N., Rautiainen, J., Rieppo, L., Saarakkala, S., Nissi, M.J., 2017. Orientation anisotropy of quantitative MRI relaxation parameters in ordered tissue. Sci. Rep. 7 (1), 1–11.

Hernández-Torres, E., Kassner, N., Forkert, N.D., Wei, L., Wiggermann, V., Daemen, M., Machan, L., Traboulsee, A., Li, D., Rauscher, A., 2017. Anisotropic cerebral vascular architecture causes orientation dependency in cerebral blood flow and volume measured with dynamic susceptibility contrast magnetic resonance imaging. J. Cereb. Blood Flow Metab. 37 (3), 1108–1119.

Hillman, E.M.C., Devor, A., Bouchard, M.B., Dunn, A.K., Krauss, G.W., Skoch, J., Bacskai, B.J., Dale, A.M., Boas, D.A., 2007. Depth-resolved optical imaging and microscopy of vascular compartment dynamics during somatosensory stimulation. Neuroimage 35 (1), 89–104.

Hirsch, S., Klatt, D., Freimann, F., Scheel, M., Braun, J., Sack, I., 2013. In vivo measurement of volumetric strain in the human brain induced by arterial pulsation and harmonic waves. Magn. Reson. Med. 70 (3), 671–682.

Hirsch, S., Reichold, J., Schneider, M., Székely, G., Weber, B., 2012. Topology and hemodynamics of the cortical cerebrovascular system. J. Cereb. Blood Flow Metab. 32 (6), 952–967.

Huber, L., Goense, J., Kennerley, A.J., Trampel, R., Guidi, M., Reimer, E., Ivanov, D., Neef, N., Gauthier, C.J., Turner, R., Möller, H.E., 2015. Cortical lamina-dependent blood volume changes in human brain at 7T. Neuroimage 107, 23–33.

Hurley, A.C., Al-Radaideh, A., Bai, L., Aickelin, U., Coxon, R., Glover, P., Gowland, P.A., 2010. Tailored rf pulse for magnetization inversion at ultrahigh field. Magn. Reson. Med. 63 (1), 51–58.

Jenkinson, M., 2004. Improving the registration of B0-distorted EPI images using calculated cost function weights. In: Tenth International Conference on Functional Mapping of the Human Brain.

Jezzard, P., Balaban, R.S., 1995. Correction for geometric distortion in echo planar images from B0 field variations. Magn. Reson. Med. 34 (1), 65–73.

Keil, B., Triantafyllou, C., Hamm, M., Wald, L., 2010. Design optimization of a 32-channel head coil at 7 T. In: Proceedings of the International Society in Magnetic Resonance in Medicine, vol. 18, p. 1493.

Kennel, P., Fonta, C., Guibert, R., Plouraboué, F., 2017. Analysis of vascular homogeneity and anisotropy on high-resolution primate brain imaging. Hum. Brain Mapp. 38 (11), 5756–5777.

Kleinfeld, D., Mitra, P.P., Helmchen, F., Denk, W., 1998. Fluctuations and stimulus-induced changes in blood flow observed in individual capillaries in layers 2 through 4 of rat neocortex. Proc. Natl. Acad. Sci. U. S. A 95 (26), 15741–15746.

Krüger, G., Glover, G.H., 2001. Physiological noise in oxygenation-sensitive magnetic resonance imaging. Magn. Reson. Med. 46 (4), 631–637.

Kundu, P., Santin, M.D., Bandettini, P.A., Bullmore, E.T., Petiet, A., 2014. Differentiating BOLD and non-BOLD signals in fMRI time series from anesthetized rats using multi-echo EPI at 11.7T. Neuroimage 102 (P2), 861–874.

Kwong, K.K., Belliveau, J.W., Chesler, D.A., Goldberg, I.E., Weisskoff, R.M., Poncelet, B.P., Kennedy, D.N., Hoppel, B.E., Cohen, M.S., Turner, R., 1992. Dynamic magnetic resonance imaging of human brain activity during primary sensory stimulation. Proc. Natl. Acad. Sci. Unit. States Am. 89 (12), 5675–5679.

Lee, J., van Gelderen, P., Kuo, L.W., Merkle, H., Silva, A.C., Duyn, J.H., 2011. T2*-based fiber orientation mapping. Neuroimage 57 (1), 225–234.

Lu, H., Golay, X., Pekar, J.J., Van Zijl, P.C., 2003. Functional magnetic resonance imaging based on changes in vascular space occupancy. Magn. Reson. Med. 50 (2), 263–274.

Menon, R.S., 2002. Postacquisition suppression of large-vessel BOLD signals in high-resolution fMRI. Magn. Reson. Med. 47 (1), 1–9.

Meyer, M., Desbrun, M., Schröder, P., Barr, A.H., 2003. Discrete differential-geometry operators for triangulated 2-manifolds. In: Visualization and Mathematics III. Springer, pp. 35–57.

Ogawa, S., Lee, T.M., Kay, A.R., Tank, D.W., 1990. Brain magnetic resonance imaging with contrast dependent on blood oxygenation. Proc. Natl. Acad. Sci. U. S. A 87 (24).

Ogawa, S., Menon, R.S., Tank, D.W., Kim, S.G., Merkle, H., Ellermann, J.M., Ugurbil, 1993. Functional brain mapping by blood oxygenation level-dependent contrast magnetic resonance imaging. A comparison of signal characteristics with a biophysical model. Biophys. J. 64 (3), 803–812.

Oh, S.H., Kim, Y.B., Cho, Z.H., Lee, J., 2013. Origin of B0 orientation dependent R2* (=1/T2*) in white matter. Neuroimage 73, 71–79.

Özbay, P.S., Chang, C., Picchioni, D., Mandelkow, H., Moehlman, T.M., Chappel-Farley, M.G., van Gelderen, P., de Zwart, J.A., Duyn, J.H., 2018. Contribution of systemic vascular effects to fmri activity in white matter. Neuroimage 176, 541–549.
Peer, M., Nitzan, M., Bick, A.S., Levin, N., Arzy, S., 2017. Evidence for functional networks within the human brain's white matter. J. Neurosci. 37 (27), 6394–6407.
Pfeifer, R.A., 1928. Die Angioarchitektonik der Grosshirnrinde. Springer, Berlin.
Polimeni, J.R., Bhat, H., Witzel, T., Benner, T., Feiweier, T., Inati, S.J., Renvall, V., Heberlein, K., Wald, L.L., 2015. Reducing sensitivity losses due to respiration and motion in accelerated echo planar imaging by reordering the autocalibration data acquisition. Magn. Reson. Med. 75 (2), 665–679.
Polimeni, J.R., Fischl, B., Greve, D.N., Wald, L.L., 2010. Laminar analysis of 7T BOLD using an imposed spatial activation pattern in human V1. Neuroimage 52 (4), 1334–1346.
Polimeni, J.R., Renvall, V., Zaretskaya, N., Fischl, B., 2018. Analysis strategies for high-resolution UHF-fMRI data. Neuroimage 168, 296–320.
Polimeni, J.R., Wald, L.L., 2018. Magnetic resonance imaging technology—bridging the gap between noninvasive human imaging and optical microscopy. Curr. Opin. Neurobiol. 50, 250–260.
Setsompop, K., Gagoski, B.A., Polimeni, J.R., Witzel, T., Wedeen, V.J., Wald, L.L., 2012. Blipped-controlled aliasing in parallel imaging for simultaneous multislice echo planar imaging with reduced g-factor penalty. Magn. Reson. Med. 67 (5), 1210–1224.
Tian, P., Teng, I.C., May, L.D., Kurz, R., Lu, K., Scadeng, M., Hillman, E.M., De Crespigny, A.J., D'Arceuil, H.E., Mandeville, J.B., et al., 2010. Cortical depth-specific microvascular dilation underlies laminar differences in blood oxygenation level-dependent functional mri signal. Proc. Natl. Acad. Sci. Unit. States Am. 107 (34), 15246–15251.
Triantafyllou, C., Hoge, R.D., Krueger, G., Wiggins, C.J., Potthast, A., Wiggins, G.C., Wald, L.L., 2005. Comparison of physiological noise at 1.5T, 3T and 7T and optimization of fMRI acquisition parameters. Neuroimage 26 (1), 243–250.
Ugurbil, K., Hu, X., Chen, W., Zhu, X.H., Kim, S.G., Georgopoulos, A., 1999. Functional mapping in the human brain using high magnetic fields. Phil. Trans. Biol. Sci. 354 (1387), 1195–1213.
Uludag, K., Mueller-Bierl, B., Ugurbil, K., 2009. An integrative model for neuronal activity-induced signal changes for gradient and spin-echo functional imaging. Neuroimage 48 (1), 150–165.
van der Kouwe, A.J.W., Benner, T., Salat, D.H., Fischl, B., 2008. Brain morphometry with multiecho MPRAGE. Neuroimage 40 (2), 559–569.
Viessmann, O., Bianciardi, M., Scheffler, K., Wald, L., Polimeni, J., 2018. The EPI rs-FfMRI signal shows an orientation effect with respect to B0 and phase-encode axis across cortical depth. In: Joint Annual Meeting ISMRM-ESMRMB, vol. 27, p. 395.
Viessmann, O., Möller, H.E., Jezzard, P., 2017. Cardiac cycle-induced EPI time series fluctuations in the brain: their temporal shifts, inflow effects and T2* fluctuations. Neuroimage 162, 93–105.
Wald, L.L., Polimeni, J.R., 2017. Impacting the effect of fMRI noise through hardware and acquisition choices–Implications for controlling false positive rates. Neuroimage 154, 15–22.
Yablonskiy, D.A., Haacke, E.M., 1994. Theory of NMR signal behavior in magnetically inhomogeneous tissues: the static dephasing regime. Magn. Reson. Med. 32 (6), 749–763.
Zaretskaya, N., Fischl, B., Reuter, M., Renvall, V., Polimeni, J.R., 2018. Advantages of cortical surface reconstruction using submillimeter 7T MEMPRAGE. Neuroimage 165, 11–26.